Journal of Power Sources 688 (2026) 240504

Contents lists available at ScienceDirect

Journal of Power Sources

journal homepage: www.elsevier.com/locate/jpowsour

Impact of water content on reversible Solid Oxide Cells: Semi-empirical modelling and effective electrolyte conductivity estimation

Francesca Mennilli [a], Mosè Rossi [a,*], Andrea Monforti Ferrario [b], Massimiliano Della Pietra [b], Gabriele Comodi [a]

[a] Marche Polytechnic University, Department of Industrial Engineering and Mathematical Sciences (DIISM), Via Brecce Bianche, 12, Ancona, 60131, Italy
[b] ENEA - Italian National Agency for New Technologies, Energy and Sustainable Economic Development, Department of Energy Technologies and Renewable Sources (TERIN), Decarbonisation (DEC), Laboratory for Hydrogen and new Energy Vectors (H2V), Via Anguillarese 301, Rome, 00123, Italy

GRAPHICAL ABSTRACT

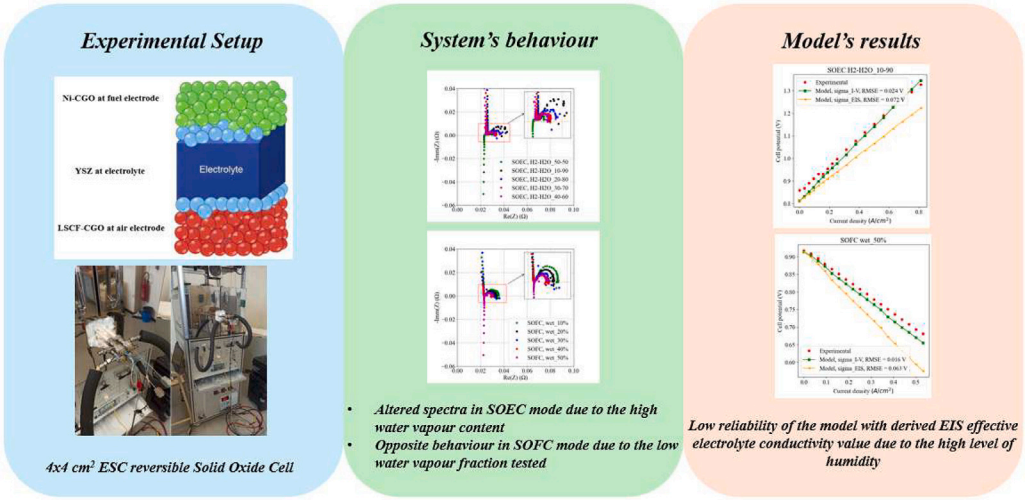

HIGHLIGHTS

- At 50% H_2O in SOEC, EIS-based σ gives RMSE of 0.0075 V vs 0.054 V from PC-based σ .
- Increasing H_2O to 90% in SOEC raised EIS-based model RMSE to 0.072 V.
- SOEC electrolyte σ from EIS dropped from 0.022 to 0.019 S/cm as H_2O rose to 90%.
- PC-derived σ also declined in SOEC, from 0.017 to 0.014 S/cm with higher H_2O.
- In SOFC mode at 50% H_2O, EIS σ (0.014 S/cm) underestimated vs PC σ (0.019 S/cm).

ARTICLE INFO

Keywords:
Electrochemical impedance spectroscopy
Effective electrolyte conductivity

ABSTRACT

Solid Oxide Cell (SOC) performance strongly depends on temperature, pressure, gas composition, and flow rate. While extensive research has focused on SOC optimisation, the impact of water content on predictive reliability remains underexplored. This study investigates how fuel-side water concentration affects reversible

* Corresponding author.
E-mail address: mose.rossi@staff.univpm.it (M. Rossi).

https://doi.org/10.1016/j.jpowsour.2026.240504
Received 6 February 2026; Received in revised form 28 April 2026; Accepted 22 May 2026
Available online 4 June 2026

Hydration effects
Reversible solid oxide cells
Semi-empirical numerical model

SOC (rSOC) performance. Effective conductivity parameters were estimated from Electrochemical Impedance Spectroscopy (EIS) and polarisation curves under different fuel compositions, showing dependence on steam content due to transport and interfacial effects. These parameters were used to calibrate a semi-empirical rSOC model. For EIS-based conductivity estimation, increasing steam content reduced predictive reliability, defined as agreement between simulated and experimental curves. In SOEC mode, Root Mean Square Error (RMSE) increased from 0.0075 V at 50% steam to 0.072 V at 90% steam, while in SOFC mode from 0.038 V at 10% steam to 0.063 V at 50% steam. These results highlight the need to account for water-content effects in rSOC modelling.

1. Introduction

The current climate change issues, due to the overexploitation of fossil fuels together with population growth, brought to light the need for alternative energy systems rather than fossil fuel-based ones. In this context, renewable energy plays a crucial role in transitioning towards a more sustainable, secure, and environmentally friendly energy model, particularly in regions with a high energy dependence. Water electrolysis through renewable energy, which is the so-called green hydrogen production, is considered one of the possible solutions to speed up the decarbonisation process as reported by [1], where the authors evaluated this process from a techno-economic point of view. In this regard, green hydrogen can serve either as an energy carrier or as a medium-term energy storage solution to enhance grid stability. Similar flexibility services can also be provided by other energy storage technologies, such as Li-ion batteries, as discussed in [2].

So far, several electrolysis/fuel cell technologies have been made available on the market. In particular, they can be sorted into two main groups based on operating temperature. Solid Oxide (SO) and Molten Carbonate (MC) are classified as High-Temperature (HT) technologies since they are operated above 100°C, while Alkaline (ALK), Anion Exchange Membrane (AEM), and Proton Exchange Membrane (PEM) are classified as Low-Temperature (LT) technologies since they operate below 100°C. Alkaline, PEM, SO, and MC are the most widely used technologies, whereas AEM is still in the development phase according to [3]. HT systems such as SO and MC present several advantages compared to LT ones according to [4], and they are reported in Table 1.

In recent years, significant attention has been directed towards SO technologies due to their greater versatility. In contrast, MC technologies rely on a highly corrosive MC electrolyte, which accelerates component degradation, shortens system lifespan, and increases operating costs. MC technologies also require a continuous external CO_2 supply to sustain internal reactions, thus complicating the Balance-of-Plant (BoP) as reported by [5,6]. On the other hand, SO technologies operate without a carbonate cycle or an external CO_2 flow, thus making them suitable for systems' integration and long-term applications. SO cells are electrochemical devices where a SO electrolyte serves as a ceramic membrane, thus allowing the passage of O_2^- ions. When operated as an electrolyser, water vapour is supplied to the cathode electrode where it is reduced to produce H_2 and O_2^- ions at the cathode-electrolyte interface. The oxide ions then migrate through the electrolyte to the anode where they are oxidised to produce O_2. These processes are described by the following chemical reactions:

$$2\,O_2^- \longrightarrow O_2 + 4\,e^- \tag{1}$$

$$2\,H_2O\,(\text{steam}) + 4\,e^- \longrightarrow 2\,H_2 + 2\,O_2^- \tag{2}$$

When operating in fuel cell mode, reverse reactions allow the production of electrical energy from hydrogen and oxygen supplied as feed gases to the cell. Both reactions are influenced by specific operating conditions such as temperature, pressure, gas composition, and flow rates. These factors induce electrochemical phenomena that, in turn, affect the system's performance; therefore, it is crucial to study the impact of varying operating conditions on the cell's behaviour. This can be evaluated by using numerical models to simulate and predict system's performance, thus reducing the need for extensive experimental testing.

Additionally, advanced techniques such as impedance spectroscopy might help identifying key electrochemical phenomena within the cell, which can further refine and improve the accuracy of the numerical models. Kim et al. [7] focused on the water content effect on Ni-CGO anodes in SO symmetrical fuel cells using the Electrochemical Impedance Spectroscopy (EIS) to study the High-Frequency (HF) and Low-Frequency (LF) impedance response of the electrodes in dry and moist atmospheres. Results showed that the moisture reduces the anode polarisation resistance and improve the cell performance, while dry conditions cause microstructural damage (e.g., crack formation) and increase LF impedance due to hindered mass transport process. Rizvandi et al. [8] realised a semi-empirical electrochemical model calibrated against experimental polarisation curves in both fuel cell (SOFC) and electrolysis (SOEC) modes. Their optimisation yielded distinct kinetic parameters: in SOFC mode, the fuel exchange current density activation energy was 125.3 kJ/mol and the oxygen exchange energy 141.1 kJ/mol, with respective pre-exponential factors of $1.47 \cdot 10^{-7}$ and $3.32 \cdot 10^{-8}$ A/m^2. In contrast, fitting polarisation curves in SOEC mode required a fuel activation energy of 148.4 kJ/mol, an oxygen activation energy of 116.8 kJ/mol, and different partial-pressure exponents (e.g., the hydrogen partial-pressure exponent changed from 0.641 (SOFC) to −0.1932 (SOEC)), highlighting mode-dependent kinetics. Using these distinct parameter sets yielded good agreement with experimental data in both operation regimes. Hoerlein et al. [9] performed a systematic long-term degradation study on 20 planar LSCF–CGO–YSZ–Ni/YSZ fuel-electrode supported cells operated for 1000 h with varied temperature (750-850°C), steam humidity (40-80 $\%MH$) and current density. They identified five separate processes by impedance spectroscopy, with ohmic resistance growth dominating overall degradation. Notably, at 800°C and 80% steam humidity, the ohmic area-specific resistance increased significantly, e.g., from 0.09 Ω cm^2 to 0.16 Ω cm^2 in related comparators under similar conditions, reflecting enhanced Ni loss at the fuel electrode/electrolyte interface. Ni depletion became significant above 800°C and 80 $\%MH$, and its severity increased with current density, correlating with microstructural evidence of Ni loss and pore expansion at the active interface.

Hauck et al. [10] realised and validated a 0D thermodynamic in Aspen Plus regarding a reversible SOFC (rSOFC) and quantified the influence of inlet gas composition, temperature, and pressure on performance. Simulation results demonstrated that adding CO_2 to the steam feed increases predicted electrolysis output via water–gas–shift reactions rather than direct CO_2 electrolysis, enhancing syngas production at given steam fractions. A parametric analysis showed that increasing inlet hydrogen fraction shifts the predicted Nernst voltage upward in fuel cell mode but raises the required cell voltage in electrolysis mode, whereas a higher steam fraction has the opposite effect. Furthermore, higher operating temperatures (e.g., approaching 900°C) improved electrolysis cell voltages and overall performance, and pressurised operation increased operational voltages while reducing diffusion losses in fuel cell mode relative to ambient pressure cases. Ihara et al. [11] investigated the effect of operating mode and fuel gas humidification on the interfacial stability of Ni/YSZ electrodes

Nomenclature

AC	Alternating Current
AEM	Anion Exchange Membrane
ALK	Alkaline
ASR	Area Specific Resistance
BoP	Balance-of-Plant
CGO	Ceria-Gadolinia Oxide
DGM	Dusty Gas Model
DRT	Distribution of Relaxation Times
EIS	Electrochemistry Impedance Spectroscopy
ESC	Electrolyte-Supported Cell
FIB	Focused Ion Beam
FRA	Frequency Response Analyser
GDC	Gadolinium-Doped Ceria
HF	High-Frequency
HT	High-Temperature
LF	Low-Frequency
$LSCF$	Lanthanum Strontium Cobalt Ferrite
$LSCN$	Lanthanum Strontium Cobalt Nickel oxide
LSM	Lanthanum Strontium Manganite
LT	Low-Temperature
MC	Molten Carbonate
MF	Mid-Frequency
MH	Mass Humidity
$MIEC$	Mix Ionic Electronic Conducting
OCV	Open Circuit Voltage
ORR	Oxygen Reduction Reaction
PC	Polarisation Curve
PEM	Proton Exchange Membrane
RES	Renewable Energy Source
$RMSE$	Root Mean Square Error
$rSOC$	reversible Solid Oxide Cell
$RWGS$	Reverse Water Gas Shift
SEM	Scanning Electron Microscope
SO	Solid Oxide
$SOEC$	Solid Oxide Electrolysis Cell
$SOFC$	Solid Oxide Fuel Cell
TPB	Triple-Phase Boundary
WGS	Water Gas Shift
YSZ	Yttria-Stabilised Zirconia

Physics constants

F	Faraday's constant (96 485 C/mol)
R	Universal gas constant (J/mol K)

Electrochemical variables

α	Charge transfer coefficient
α_i	Charge transfer coefficient of electrode i
δ_{O_2}	Dimensionless coefficient
γ	Pre-exponential factor (A/cm^2)
γ_i	Pre-exponential factor of electrode i (A/cm^2)
μ	Dynamic viscosity (Pa s)
ω	Angular frequency (rad/s)
ϕ	Current phase angle (rad)
σ_0	Reference electrolyte conductivity (S/cm)
σ_{el}	Electrolyte conductivity (S/cm)
τ	Electrode tortuosity
θ	Voltage phase angle (rad)
ε	Electrode porosity
A	Empirical constant for viscosity correlation
A_{cell}	Cell area (cm^2)
B	Empirical constant for viscosity correlation
B_g	Flow permeability
C	Empirical constant for viscosity correlation
D	Empirical constant for viscosity correlation
$D^{eff}_{H_2O}$	Water effective diffusion coefficient on the electrode (m^2/s)
$D^{eff}_{H_2}$	Hydrogen effective diffusion coefficient on the electrode (m^2/s)
$D^{eff}_{O_2}$	Oxygen effective diffusion coefficient on the electrode (m^2/s)
d_{H_2}	Fuel electrode thickness (m)
d_{O_2}	Air electrode thickness (m)
E	Empirical constant for viscosity correlation
E	Voltage amplitude (V)
$E_{act,i}$	Reaction activation energy of electrode i (J/mol)
E_{act}	Reaction activation energy (J/mol)
E_a	Electrolyte activation energy (J/mol)
E_{OCV}	Open Circuit Voltage (V)
E_{rev}	Reversible potential (V)
F	Empirical constant for viscosity correlation
f	Frequency (Hz)
G	Empirical constant for viscosity correlation
H	Empirical constant for viscosity correlation
I	Current amplitude (A)
i	Current density (A/cm^2)
$i_{0,i}$	Exchange current density of electrode i (A/cm^2)
i_0	Exchange current density (A/cm^2)
n	Number of electrons exchanged (2)
n_i	Number of electrons exchanged at electrode i
N_c	Number of cells
$P^0_{H_2O}$	Partial pressure of vapour produced at the electrode surface (Pa)
$P^0_{H_2}$	Hydrogen partial pressure at the fuel electrode outlet (Pa)
$p^0_{O_2}$	Oxygen partial pressure at the air electrode outlet (Pa)
P_{H_2O}	Partial pressure of water vapour (Pa)

in SO cells. Model Ni thin-film electrodes on dense YSZ electrolytes were tested at 1000°C under SOFC and SOEC operation using humidified hydrogen with 10–80% H_2O. Electrochemical characterisation was performed through polarisation curves and EIS, complemented by post-test microstructural analysis. While the Ni/YSZ contact angle remained nearly constant (≃113°) under open-circuit conditions, significant changes were observed under polarisation. During the SOFC operation with 80% H_2O, the contact angle decreased to 67–87°, indicating improved wettability, whereas during SOEC operation with 10% H_2O it increased to 118–129°, suggesting reduced interfacial adhesion. Impedance results showed that these effects mainly influenced the polarisation resistance, while the ohmic resistance remained nearly

P_{H_2}	Partial pressure of hydrogen (Pa)
P_{O_2}	Partial pressure of oxygen (Pa)
p_o	Pressure at the oxygen electrode (Pa)
P_{tot}	Total operating pressure (Pa)
R_0	Ohmic resistance from EIS (Ω)
R_p	Polarisation resistance from EIS (Ω)
R_{int}	Internal cell resistance (Ω)
R_{ohm}	Ohmic resistance (Ω)
r_p	Mean pore radius (m)
s	Electrolyte thickness (cm)
t	Time (s)
T	Cell temperature (K)
T_{ref}	Reference temperature (K)
V	Cell potential (V)
$V_{act,a}$	Anode activation overpotential (V)
$V_{act,c}$	Cathode activation overpotential (V)
V_{act}	Activation overpotential (V)
V_{conc}	Concentration overpotential (V)
V_{ohm}	Ohmic overpotential (V)
x_i	Molar fraction of species i
$Z''(\omega)$	Imaginary part of impedance (Ω)
$Z'(\omega)$	Real part of impedance (Ω)
$Z^*(\omega)$	Complex impedance (Ω)

Table 1
Advantages and disadvantages of high-temperature (HT) electrochemical systems (SO and MC).
Source: Adapted from [4].

Advantages	Disadvantages
At high temperatures, part of the energy required for the reaction can be supplied as heat, reducing electrical input and enhancing overall energy efficiency.	Requirement for specialised materials capable of withstanding high-temperature operation.
Electrical efficiency exceeding 90% under optimal operating conditions.	High system and material costs.
Potential to utilise waste heat from industrial processes, further increasing overall system efficiency.	Material degradation under harsh operating conditions.
Enhanced kinetics of electrochemical reactions due to high-temperature operation.	Limited operational lifetime.
Capability to operate in both electrolysis and fuel cell modes, enabling effective integration with renewable energy sources.	–

unchanged, highlighting the strong impact of operating conditions on interfacial phenomena and electrode stability. Grimes et al. [12] studied the effect of Gadolinium-Doped Ceria (GDC) infiltration into Ni-YSZ fuel electrodes for reversible SO cell operation. Electrochemical characterisation based on impedance spectroscopy under both SOFC and SOEC conditions showed an approximately 50% reduction in the initial polarisation resistance due to GDC infiltration, mainly associated to a decrease in charge-transfer-related impedance in the 100–1000 Hz frequency range. Long-term reversible tests at 700–800°C and current densities up to ±0.75 A/cm^2 revealed significantly reduced degradation rates, with voltage degradation of about 5.2–5.5% ΔV/kh for infiltrated cells compared to 10.7% ΔV kh^{-1} for non-infiltrated ones. Microstructural analysis further indicated that GDC infiltration mitigates Ni coarsening, limiting the Ni particle size increase to approximately 14% after 1000 h at 800°C, compared to about 23% in non-infiltrated electrodes.

Silva et al. [13] realised a multiscale model for SO cells that couples detailed electrochemical kinetics, gas diffusion, and explicit microstructural influences to rigorously link local electrode phenomena with global cell response. The model was validated against dedicated polarisation curve measurements at 700°C, 750°C, and 800°C in both SOFC and SOEC modes, showing excellent agreement between simulated and measured voltages across the entire current density range, with deviations typically within a few tens of millivolts. In stacked cell tests, the model reproduced experimental trends such as a 0.3 V difference at 0.3 A/cm^2 between rich and poor hydrogen compositions in SOFC mode and 0.4 V at −0.3 A/cm^2 in SOEC mode. The overall model predictions fell within <4% error of measurements in both operation regimes, and fitted kinetic parameters (e.g., activation energies on the order of 100-120 kJ/mol) captured operating-mode-dependent changes in adsorption and charge-transfer pathways at both electrodes. These quantitative validations demonstrate that the multiscale framework accurately captures the spatial and mechanistic variations governing SOC performance. Zheng et al. [14] investigated the electrochemical performance and durability of a $La_{0.8}Sr_{0.2}Co_{0.8}Ni_{0.2}O_{3-\delta}$ (LSCN)-impregnated oxygen electrode for H_2O/CO_2 co-electrolysis in SO electrolysis cells. A nanostructured LSCN-impregnated GDC-LSM composite oxygen electrode was comparatively analysed against a conventional GDC-LSM electrode in both SOFC and SOEC modes, under varying operating conditions including temperature, applied voltage, and feed gas composition. The LSCN-impregnated cell exhibited enhanced electrochemical performance, achieving a peak power density of 1057 mW/cm^2 at 800°C in SOFC mode and a current density of 1.60 A/cm^2 at 1.5 V and 800°C during H_2O/CO_2 co-electrolysis (H_2O/CO_2 = 2:1). Impedance spectroscopy and polarisation curve analyses showed that performance improves with increasing steam content, with H_2 mainly produced via steam electrolysis and CO predominantly formed through RWGS/WGS reactions. Long-term tests demonstrated stable operation for more than 100 h, while degradation under high current density was mainly attributed to coarsening of LSCN nanoparticles in the oxygen electrode. Song et al. [15] investigated the degradation of Ni-YSZ fuel electrodes subjected to redox cycling by combining electrochemical impedance spectroscopy with detailed microstructural and mechanical analyses. Up to 20 redox cycles at 800°C were analysed using EIS, Focused Ion Beam-Scanning Electron Microscope (FIB-SEM) tomography, nanoindentation and physically based modelling to correlate polarisation resistance with Triple-Phase Boundary (TPB) evolution. The TPB density decreased from 4.63 to 1.06 μm^{-2}, leading to an overall increase in polarisation resistance by about one order of magnitude, despite transient resistance reductions after re-reduction due to temporary Ni nanoparticles formation. Redox cycling also caused irreversible mechanical degradation, with hardness decreasing from 0.40 to 0.15 GPa and elastic modulus from 36.4 to 20.2 GPa. The results demonstrated that repeated Ni volume changes, Ni agglomeration and YSZ framework fracture are the primary drivers of coupled electrochemical and mechanical degradation in Ni-YSZ electrodes.

Martos et al. [16] analysed the electrochemical performance of SO cell stacks manufactured using additive manufacturing techniques. rSOFC/rSOEC stacks based on 3D-printed, complex-shaped electrolyte-supported cells were fabricated and characterised, embedding interconnector functionality directly into the cell design to reduce stack volume and weight by up to threefold and fourfold, respectively. Substacks and full stacks were tested at 900°C, delivering up to 27 W (200 mW/cm^2) in SOFC mode and reaching injected currents of −20 A in SOEC mode, with full stacks achieving power levels of about 330 W. Long-term operation exceeding 500 h showed limited degradation of approximately 5%, demonstrating the durability and scalability of additively manufactured SOC stacks with enhanced power density and mechanical robustness. Pagliari et al. [17] studied the influence of gas composition on the electrochemical performance and durability of SO cells using electrochemical impedance spectroscopy. Applicative-size anode-supported SOFCs were operated for more than 1000 h

under CO_2-rich oxidising conditions (21% O_2–79% CO_2) relevant to the SO semi-closed CO_2 cycle, and compared with conventional air operation using both humidified H_2 and reformate fuels. Replacing air with the O_2/CO_2 mixture caused a reversible power density reduction, from 672 to 508 mW/cm^2 at 0.7 V under humidified H_2, while stable operation without permanent degradation was observed. EIS and Distribution of Relaxation Times (DRT) analyses demonstrated that CO_2 mainly induces a kinetic inhibition of the Oxygen Reduction Reaction (ORR), allowing the extraction of ORR rate dependencies on O_2 and CO_2 partial pressures and confirming the feasibility of SOC operation under CO_2-rich conditions. Akter et al. [18] investigated the electrochemical performance and long-term stability of rSOCs operated under different regimes, comparing continuous SOEC operation with reversible SOFC/SOEC cycling. Single cells were experimentally characterised under potentiostatic conditions using polarisation curves, EIS and DRT analysis, supported by post-test microstructural observations. Results showed that continuous electrolysis leads to pronounced performance degradation, whereas reversible operation significantly mitigates degradation and improves electrochemical stability. Impedance and microstructural analyses indicated that degradation mechanisms are mainly associated with transport and microstructural changes in the fuel electrode, while the oxygen electrode remains largely stable. The study highlights reversible operation as an effective strategy to enhance rSOC durability. Wang et al. [19] used impedance spectra to assess the performance and durability of LT rSOCs (LT-SOCs) operating between 450–600°C, when varying the fuel H_2/H_2O composition. In particular, they found that the HF arc decreased with increasing temperature due to a better ionic conductivity in the electrolyte, and increased with a higher H_2O concentration possibly due to the partial oxidation of Ni to NiO. The Mid-Frequency (MF) arc size decreased with increasing temperature and H_2O content, thus suggesting faster reaction rates at elevated temperatures, while the LF arc decreased from 450 to 500°C and increased from 550 to 600°C, probably due to improved electrode activity and concentration polarisation.

Although previous studies extensively investigated SOC performance, degradation mechanisms, humidity effects, and electrochemical characterisation, limited attention has been devoted to how variations in fuel-side water content affect the consistency of conductivity estimation methods and how these uncertainties propagate into semi-empirical model accuracy. In particular, comparative assessments between EIS- and polarisation-derived conductivity parameters under varying steam contents remain scarce, especially for reversible operation in both SOEC and SOFC modes. Since EIS provides process-resolved information whereas polarisation curves reflect the global voltage response of the cell, comparing conductivity parameters derived from both methods may help identify the most reliable calibration strategy under varying steam contents. This research work aims to fill this gap by systematically analysing the influence of water concentration in the fuel mixture of a single-cell rSOC on electrolyte conductivity assessment. In particular, conductivity values derived from both EIS and polarisation curve measurements under different fuel gas compositions are compared and subsequently implemented within a rSOC semi-empirical numerical model. The objective is to quantify how water content affects the robustness, consistency, and predictive reliability of single-cell rSOC numerical modelling in both SOEC and SOFC operating modes. Although the present work is focused on cell-level analysis, the proposed methodology may also support future stack-level simulations and higher-level digital twin frameworks through improved parameter calibration.

The paper is structured as follows: Section 2 provides a complete overview of the rSOC system tested along with the EIS principles, the experimental campaign performed, and the proposed semi-empirical numerical model. Section 3 shows and discusses the results, highlighting how the different values of the electrolyte conductivity obtained either from polarisation curves or EIS spectra affect the reliability of the proposed semi-empirical numerical model. Finally, Section 4 reports the conclusions of the work and its possible future developments.

2. Materials and methods

In this section, a detailed description of EIS principles, the rSOC system used, the experimental campaign performed, and the proposed semi-empirical model developed is provided.

2.1. EIS principles

EIS is a sensitive technique that studies the response of an electrochemical device to the application of a periodic small Alternating Current (AC) signal carried out at different frequencies. In contrast to polarisation curves, EIS measurements can shed light on the different physio-chemical processes occurring in the active layers of an electrochemical cell by exploiting their inherent nature; indeed, each process has a unique time-constant, also named as relaxation time, which shows up at different frequencies [20]. If the studied system satisfies contemporaneously the conditions of causality, linearity, and time invariance, the response to a sinusoidal voltage (or current) excitation signal will be a sinusoidal current (or voltage) signal, both sharing the same frequency. As a consequence, for the generic sinusoidal voltage input signal reported in Eq. (3), the response is a sinusoidal signal that can be expressed through Eq. (4), where $\omega = 2 \cdot \pi \cdot f$ is the frequency of the signal, E and I are the amplitude of the voltage and current signals, respectively, and θ and ϕ are their initial phases [21]:

$$e(t) = E \cdot cos(\omega \cdot t + \theta) \tag{3}$$

$$i(t) = I \cdot cos(\omega \cdot t + \phi) \tag{4}$$

Both expressions can be reshaped as complex-form functions through Eqs. (5) and (6):

$$e^*(t) = E \cdot exp[i \cdot (\omega \cdot t + \theta)] \quad \text{with} \quad e(t) = Re[e^*(t)] \tag{5}$$

$$i^*(t) = I \cdot exp[i \cdot (\omega \cdot t + \phi)] \quad \text{with} \quad i(t) = Re[i^*(t)] \tag{6}$$

When analysing an EIS spectrum, the main used parameter is the impedance, which is defined as the ratio between the complex voltage and current variables. Its mathematical form is expressed by Eq. (7):

$$Z^*(\omega) = \frac{e^*(t)}{i^*(t)} = \frac{E}{I} \cdot exp[i \cdot (\theta - \phi)] = \frac{E}{I} \cdot (cos(\theta - \phi) + i \cdot sin(\theta - \phi)) \tag{7}$$

Although being a complex variable, it can be observed how the impedance is composed of a real and an imaginary part as expressed in Eqs. (8) and (9), respectively:

$$Re[Z^*(\omega)] = Z'(\omega) = \frac{E}{I} \cdot cos(\theta - \phi) \tag{8}$$

$$Im[Z^*(\omega)] = Z''(\omega) = \frac{E}{I} \cdot sin(\theta - \phi) \tag{9}$$

SOCs exhibit different mechanisms and processes during their operation, making them non-linear systems. However, if the amplitude of the excitation signal is small enough (e.g., E <10 mV), the response of the system will be assumed linear, causal, and time-invariant [22]: this means that all the above mathematical properties are valid. EIS measurements are carried out in a defined range of frequencies and for a finite number of points; indeed, measurements should be performed from high frequencies (ca. 100 kHz) to very low frequencies (ca. 10 mHz or below) and at short intervals (at least 10 points recorded per frequency decade on a logarithmic scale) to obtain information of the phenomena occurring within the cell [22]. In this regard, the Frequency Response Analyser (FRA) imposes a small amplitude AC signal to the electrochemical cell and measures the amplitude of the response signal and the phase shift between voltage and current. The output signal from the cell is then divided into a real and an imaginary part to generate a Nyquist plot as shown in Fig. 1.

In the latter, two main resistances are identified, namely the internal R_0 and the polarisation resistance R_p. The first one is associated

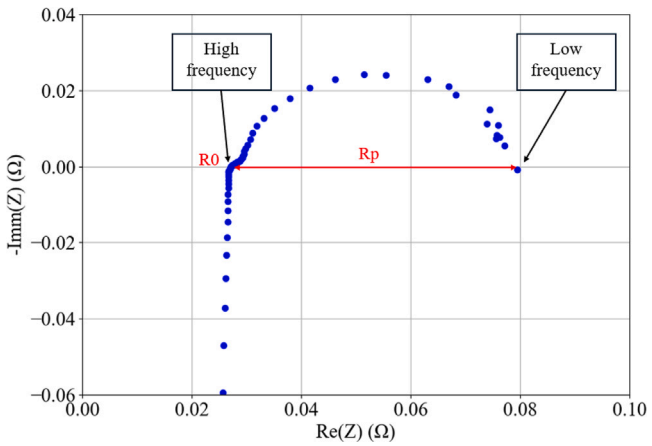

Fig. 1. EIS spectrum of a SOC.

with ohmic losses occurring within the cell, predominantly related to electrolyte ionic transport, while also including contact and interfacial contributions. However, some overlap with fast electrode polarisation processes cannot be fully excluded, especially when characteristic time constants are close. The second one is related to anodic and cathodic activation losses together with mass transport losses. Both parameters, which are measurable on the X-axis, represent the main information provided by an EIS spectrum with which it is possible to evaluate the extent of the phenomena occurring within the electrochemical cell, as well as any degradation phenomenon over time. The imaginary part of the impedance, which is located on the Y-axis, represents the system's capacitive reactance due to the double-layer that forms at the electrode-electrolyte interface. In this case, information regarding the capacitance of the double-layer along with details on the kinetics of charge and mass transfer processes are retrieved.

2.2. rSOC system and experimental campaign description

The experimental campaign was performed in the research centre of Casaccia, ENEA (National Agency for New Technologies, Energy, and Sustainable Economic Development) in the TERIN-DEC-H2V (Energy Technologies and Renewable Resources, Decarbonisation, Hydrogen and other carriers) department using a dedicated test bench, which is shown in Fig. 2(a), equipped with a furnace, electric load, pipelines for gas distribution, and gas tanks. Fig. 2(b) shows the cell's fuel and air electrodes made of a 25 μm Ni-CGO layer and a 30–35 μm LSCF-CGO perovskite layer, respectively, which are separated by a 80–85 μm dense YSZ electrolyte layer. As can be noticed, the electrolyte is the thickest layer: this means that it provides the mechanical support to the cell that is defined an Electrolyte Supported Cell (ESC). It is worth noting that the rSOC investigated in this study is a commercially available cell. Consequently, the fuel and air electrodes were not fabricated within the scope of this work, and detailed information regarding material synthesis routes, manufacturing procedures, and proprietary processing parameters is not publicly disclosed by the manufacturer. Nevertheless, to ensure transparency and reproducibility at the system and modelling level, all available information provided by the manufacturer, namely the cell architecture, constituent materials, and layer thicknesses, has been explicitly reported and consistently adopted throughout the analysis. In addition, the microstructural parameters required for the semi-empirical model, including electrode porosity and tortuosity, are explicitly reported in Table 5.

Table 2 reports the main characteristics of the used cell. Two experimental campaigns were defined, where the latter is operated in both electrolyser and fuel cell mode. In particular, gas compositions at the fuel electrode were properly varied, starting from the reference operating conditions reported in Table 3, in both SOEC and SOFC operating modes.

Starting from the above-mentioned reference conditions, the water content at the fuel electrode was gradually varied, while all the other parameters were kept fixed. In this way, the system has one degree of freedom, thus ensuring an easier controllability from a technical point of view. Table 4 reports all the variations performed for both SOEC and SOFC operating modes. All gas composition percentages reported in this work refer to volumetric fractions, which were controlled through mass flow controllers under the test bench operating conditions.

As can be noticed, the water content was gradually increased in SOEC mode to study its effect on the cell's performance; at the same time, the hydrogen concentration was decreased to maintain the same flow rate. This could negatively affect the cell's performance; indeed, since the SOC is made of a non-conductive material (Ni-CGO), a fixed input hydrogen quantity is always needed to remove the oxygen and maintain a reductive atmosphere at the fuel electrode. In this case, the catalytic properties of the electrode are preserved and the electrochemical reaction within the cell occur properly. This condition must be kept for the whole experimental campaign to prevent a re-oxidation of the electrode, which can cause structural issues over time. Furthermore, no fixed minimum hydrogen concentration threshold was imposed or identified, as the present study does not aim to determine critical reduction limits but rather to analyse system-level performance trends under controlled gas composition variations. Notably, no anomalous voltage behaviour or irreversible degradation phenomena were observed during the tests, indicating that the selected gas compositions ensured stable operation within the investigated range. The selected inlet flow rates were designed to moderate reactant utilisation. Nevertheless, at the highest investigated current densities, fuel and steam utilisation factors increased sufficiently to justify retaining concentration overpotential terms in the model.

In SOFC mode, wet conditions were tested to evaluate the cell's performance when operating with humidified hydrogen, which is a common condition in the industrial sector. In this case, nitrogen has also been used as a complementary element to achieve the wanted concentration and maintain the same flow rate. The experimental campaign was specifically designed to isolate the effect of fuel gas water content on effective electrolyte conductivity parameter estimation and assess how this variability propagates into the performance and reliability of the semi-empirical rSOC numerical model.

2.3. rSOC semi-empirical numerical model

A semi-empirical numerical model was proposed and used to account for the different gas compositions in SOEC and SOFC operating modes. The model assumes steady-state operation, lumped cell behaviour, uniform operating temperature, and voltage losses represented through activation, ohmic, and concentration terms.

The main performance curve of an electrolyser/fuel cell is the polarisation one that represents the relationship between the current density and the cell potential, as expressed by Eqs. (10) and (11) in SOFC and SOEC operating modes, respectively.

$$V_{cell} = N_c \cdot (E_{OCV} - V_{act,a} - V_{act,c} - V_{ohm} - V_{conc}) \tag{10}$$

$$V_{cell} = N_c \cdot (E_{OCV} + V_{act,a} + V_{act,c} + V_{ohm} + V_{conc}) \tag{11}$$

where N_c is the number of electrochemical cells, E_{OCV} (V) is the OCV, $V_{act,a}$ (V) and $V_{act,c}$ (V) are the anode and cathode activation overpotentials, respectively, V_{ohm} (V) is the ohmic overpotential and V_{conc} (V) is the concentration overpotential. The latter occurs at high current densities when the reaction rate is slowed down by the overpopulation of reacting molecules. In the investigated operating range, ohmic losses were found to be the dominant contribution over a large portion of the polarisation curves, although concentration effects were retained in

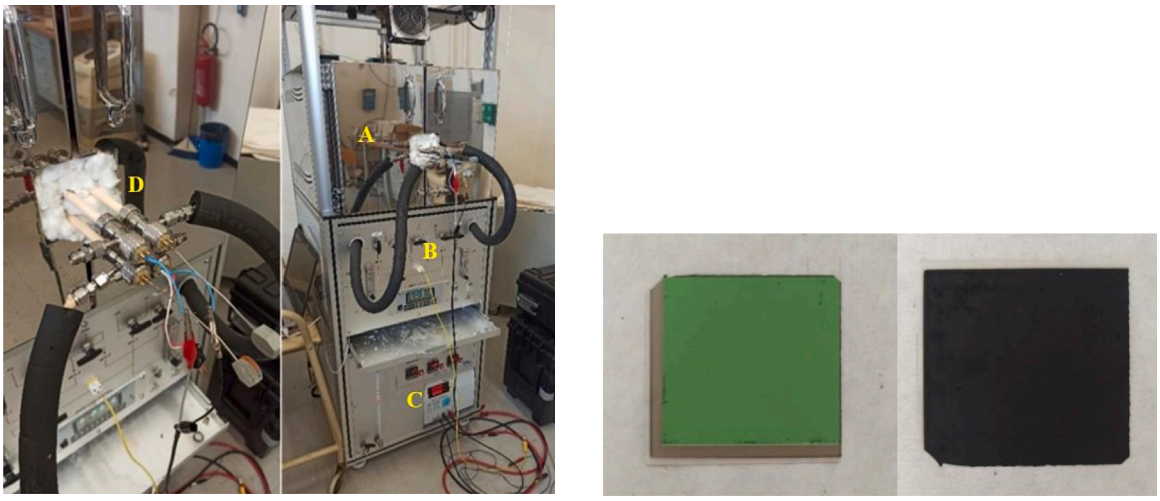

(a) (b)

Fig. 2. Experimental setup for SOC testing: (a) test bench including furnace (A), gas control valves (B), electric load (C), and cell housing (D); (b) Cell's fuel (left) and air (right) electrodes.

Table 2
SOC characteristics.

Cell type	Active area (cm^2)	Geometric area (cm^2)	Rated temperature (°C)	Rated current density (A/cm^2)	Fuel Electrode thickness (μm)	Air Electrode thickness (μm)	Electrolyte thickness (μm)
ESC	16	25	850	0.25	25	30–35	80–85

Table 3
Reference operating conditions for SOEC and SOFC mode.

	Fuel flow rate (ml/min)	Air flow rate (ml/min)	H_2 content (%)	N_2 content (%)	H_2O content (%)	Cell temperature (°C)
SOFC mode	300	800	50	50	–	850
SOEC mode	300	800	50	–	50	850

Table 4
rSOC experimental campaign.

SOEC mode	Var. % H_2–H_2O:	50–50	40–60	30–70	20–80	10–90
SOFC mode	Wet Var. % N_2–H_2–H_2O:	40-50-10	30-50-20	20-50-30	10-50-40	0-50-50

the model and may become more relevant at higher current densities depending on fuel composition.

The OCV, also known as Nernst voltage, was calculated with the Nernst equation from [23] by considering the molar concentration of the gas species and the overall pressure that was, in this case, the same in both electrodes and equal to 1 bar.

$$E_{OCV} = E_{rev}(T,p) + \frac{R\cdot T}{n\cdot F} ln \frac{P_{H_2}\cdot {P_{O_2}}^{0.5}}{P_{H_2O}} \simeq E_{rev}(T,p) + \frac{R\cdot T}{n\cdot F} ln \frac{x_{H_2}\cdot {x_{O_2}}^{0.5}}{x_{H_2O}} + \frac{R\cdot T}{2\cdot n\cdot F} ln P_{tot} \quad (12)$$

where P_x (Pa) is the partial pressure of reactants/products, T (K) is the cell temperature, F (C/mol) is the Faraday constant, R (J/mol K) is the universal gas constant, n is the number of transferred electrons during the reaction, x is the molar fraction of reactants/products, P_{tot} (Pa) is the overall operating pressure and $E_{rev}(T,p)$ (V) is the reversible cell potential at real pressure and temperature conditions, that is calculated using Eq. (13) according to [24]:

$$E_{rev}(T,p) = 1.5241 - (1.2261\cdot 10^{-3})\cdot T + (1.1858\cdot 10^{-5})\cdot T\cdot ln(T) + (5.6692\cdot 10^{-7})\cdot T^2 \quad (13)$$

As can be noticed, Eq. (13) involves only the temperature dependency; indeed, the overall pressure contribution was neglected in this case since the pressure has been kept constant for the whole experimental campaign and equal to the 1 bar as previously mentioned.

The activation losses are due to the charge transfer between electronic and ionic conductors, and represent an energy barrier that must be overcome to activate the electrochemical processes. The main equation describing the activation overpotential is the Butler-Volmer one according to [25]. Since it cannot be solved explicitly, several explicit approximations were assumed. While some of the assumptions, such as the Tafel equation from [25], are valid in specific regions of the polarisation curve, the so-called hyperbolic sine approach of [10] was used to perform well throughout the operating regions:

$$V_{act,i} = \frac{R\cdot T}{n_i\cdot F\cdot \alpha_i} sinh \frac{i}{2\cdot i_{0,i}} \quad (14)$$

where n_i is the number of the transferred electrons during the reaction (2 for the fuel electrode and 4 for the air one), α_i is the charge transfer coefficient, i (A/cm^2) is the current density and $i_{0,i}$ (A/cm^2) is the exchange current density. The index "i" stands for either the fuel, or the air electrode. The exchange current density is defined as the reaction rate at equilibrium and depends on material properties and operating conditions. Furthermore, its values are different in fuel and oxygen

side electrodes. While slightly different approaches in the exchange current density calculation can be found in the scientific literature, the Arrhenius type relation is usually used according to [10]:

$$i_{0,i} = \gamma_i \cdot exp\frac{-E_{act,i}}{R \cdot T} \tag{15}$$

where the pre-exponential factor γ_i (A/cm^2) and activation energy $E_{act,i}$ (J/mol) are empirical values.

Ohmic losses are not only due to the electric charge transport, but also to the ionic current of O_2^- through the electrolyte layer according to [10]. The main equation for the ohmic overpotential calculation is the Ohm law:

$$V_{ohm} = R_{ohm} \cdot I \tag{16}$$

where R_{ohm} (Ω) is the ohmic resistance due to the connectors, cell's metallic components (e.g., electrodes, bipolar plates), and electrolyte. The resistance to the ions transport through the electrolyte is, in general, much higher than the one occurring for electrons in an electronic conductor; for this reason, the latter is neglected considering only the electrolyte contribution [26] through an Arrhenius form like in [10]:

$$\sigma = \sigma_0 \cdot \left[\left(\frac{-E_a}{R}\right) \cdot \left(\frac{1}{T} - \frac{1}{T_{ref}}\right)\right] \tag{17}$$

where σ_0 (S/cm) is the reference electrolyte conductivity at the cell's reference temperature, E_a (J/mol) is the electrolyte activation energy, and T_{ref} (K) is the cell's reference temperature. It is worth noting that, in this work, the reference conductivity parameter was evaluated using results from both EIS and polarisation curve measurements. For the EIS-based approach, the high-frequency intercept was directly extracted from the experimental spectra without applying additional corrections to separate contact or parasitic contributions. Therefore, the EIS-derived conductivity should be interpreted as an effective fitting parameter rather than a purely intrinsic YSZ conductivity.

The polarisation curve-derived conductivity was obtained by calculating the cell's internal resistance R_{int} (Ω) from the linear slope of the experimental data. Since the recorded curves were approximately linear over the investigated operating range, activation and concentration losses were considered comparatively limited with respect to ohmic contributions. Therefore, the full set of measured points was used for slope estimation as follows:

$$R_{int} = \frac{\Delta V}{\Delta I} \tag{18}$$

$$\sigma_0 = \frac{s}{R_{int} \cdot A_{cell}} \tag{19}$$

where s (cm) is the electrolyte's thickness and A_{cell} (cm^2) is the cell's active area. Finally, the ohmic overpotential was evaluated as follows:

$$V_{ohm} = \frac{s}{\sigma} \cdot i \tag{20}$$

The concentration (or diffusion) overpotential is due to the inefficiencies related to the transport of reactant species approaching the reaction sites and product species leaving the reaction sites. Both Fick model and Dusty Gas Model (DGM) are frequently used to describe gas transport within porous media [27]. DGM is based on Stefan-Maxwell equations and includes Knudsen diffusion; however, no analytical expressions are generally available, and numerical methods are required. In comparison, the Fick model provides a simpler yet effective description of gas transport characteristics, while allowing analytical solutions. For this reason, and consistently with the semi-empirical scope of the present work, the Fick-based formulation was adopted as a suitable compromise between physical representativeness and modelling simplicity. The equations distinguished by mode and electrode are the following [28]:

$$V_{\text{conc,fuel}}^{\text{SOFC}} = -\frac{RT}{2F} \ln\left[\frac{\left(1 - \frac{R \cdot T \cdot i \cdot d_{H_2}}{2 \cdot F \cdot D_{H_2}^{\text{eff}} \cdot p_{H_2O}^0}\right)}{\left(1 + \frac{R \cdot T \cdot i \cdot d_{H_2}}{2 \cdot F \cdot D_{H_2}^{\text{eff}} \cdot p_{H_2}^0}\right)}\right] \tag{21}$$

$$V_{\text{conc,fuel}}^{SOEC} = \frac{RT}{2F} \ln\left[\frac{\left(1 + \frac{R \cdot T \cdot i \cdot d_{H_2}}{2 \cdot F \cdot D_{H_2O}^{\text{eff}} \cdot P_{H_2}^0}\right)}{\left(1 - \frac{R \cdot T \cdot i \cdot d_{H_2}}{2 \cdot F \cdot D_{H_2O}^{\text{eff}} \cdot P_{H_2O}^0}\right)}\right] \tag{22}$$

$$V_{\text{conc, air}}^{\text{SOFC}} = -\frac{RT}{4F} \ln\left[\frac{\left(\frac{p_o}{\delta_{o_2}} - \left(\frac{p_{o_2}}{\delta_{o_2}}\right) - p_{o_2}^0\right) \exp\left(\frac{RT}{4F}\left(\frac{i \cdot \delta_{o_2} \cdot d_{o_2}}{D_{o_2}^{\text{eff}} \cdot r_o}\right)\right)}{p_{o_2}^0}\right] \tag{23}$$

$$V_{\text{conc,air}}^{\text{SOEC}} = \frac{RT}{4F} \ln\left[\frac{\sqrt{(P_{O_2}^0)^2 + (i \cdot R \cdot T \cdot \mu \cdot d_{O_2})/(2 \cdot F \cdot B_g)}}{P_{O_2}^0}\right] \tag{24}$$

where $P_{H_2}^0$ (Pa) is the hydrogen partial pressure at the fuel electrode outlet, $D_{H_2}^{\text{eff}}$ (m^2/s) is the hydrogen effective diffusion coefficient on the electrode, $D_{H_2O}^{\text{eff}}$ (m^2/s) is the water effective diffusion coefficient on the electrode, d_{H_2} (m) is the fuel electrode thickness, $P_{H_2O}^0$ (Pa) is the partial pressure of vapour produced at the electrode surface, i (A/cm^2) is the current density, T (K) is the cell temperature, R (J/mol K) is the universal gas constant, F (C/mol) is the Faraday constant, p_o (Pa) is the pressure at the oxygen electrode, $p_{O_2}^0$ (Pa) is the oxygen partial pressure at the air electrode outlet, d_{O_2} (m) is the air electrode thickness, $D_{O_2}^{\text{eff}}$ (m^2/s) is the oxygen effective diffusion coefficient on the electrode, δ_{O_2} is a dimensionless coefficient, B_g is the flow permeability, and μ (Pa s) is the dynamic viscosity. For both SOFC and SOEC modes, the model was solved under prescribed operating temperature, inlet gas composition, total flow rate, and current density, while the corresponding cell voltage was calculated from the polarisation equations.

All the empirical parameters used for the overpotentials calculation are shown in Table 5 together with their reference values. Exchange current density and diffusion-related parameters were not recalibrated for each humidity condition. Their reference values were kept constant, with temperature dependence applied where appropriate, while humidity effects were accounted for through changes in gas composition and partial pressures.

3. Results and discussion

The results presented in this section are discussed by focusing on how electrolyte conductivity values extracted from EIS and polarisation curve measurements affect the predictive capability and robustness of the semi-empirical rSOC numerical model.

3.1. Experimental campaign results

As mentioned in Section 2, experimental tests were performed in both SOEC and SOFC modes by varying the water content in the fuel electrode while keeping fixed all the other parameters. In this way, the system has one degree of freedom, thus ensuring an easier control from a technical point of view. For each test, a polarisation curve together with an EIS spectrum was recorded to study the cell's response to the different operating conditions. Fig. 3 shows the EIS spectra recorded in OCV at reference conditions in SOEC and SOFC modes. It can be observed that both spectra appear free from anomalous features, as the reference condition corresponds to a safe operating mode selected to avoid cell damage during operation. For consistency with common SOC literature practice, the EIS resistances were also expressed as Area Specific Resistances (ASR), calculated using the active cell area of 16 cm^2, thus removing the influence of cell area on resistance comparisons, although the same cell geometry was used throughout the entire experimental campaign. Furthermore, it is worth noting that, even if the spectra refer to the same reference operating condition, they were recorded at two different timings of the experimental campaign, thus justifying the different values of 0.023 and 0.027 Ω of internal

Table 5
Model parameters adopted in the present study.

Parameter	Value	Reference
Pre-exponential factor (fuel electrode)	$1.34 \cdot 10^{6}$ (A/cm^2)	[10]
Pre-exponential factor (air electrode)	$2.05 \cdot 10^{7}$ (A/cm^2)	[10]
Charge transfer coefficient (fuel and air electrode)	0.5	[10]
Activation energy (fuel electrode)	99,000 (J/mol)	[29]
Activation energy (air electrode)	119,000 (J/mol)	[29]
Electrolyte activation energy	104,204 (J/mol)	[29]
Electrolyte thickness	$80 \cdot 10^{-6}$ (m)	From manufacturer
Molecular weight of hydrogen	$2 \cdot 10^{-3}$ (kg/mol)	[30]
Molecular weight of water	$18 \cdot 10^{-3}$ (kg/mol)	[30]
Molecular weight of oxygen	$32 \cdot 10^{-3}$ (kg/mol)	[30]
Molecular weight of nitrogen	$28 \cdot 10^{-3}$ (kg/mol)	[30]
Air electrode thickness	$30 \cdot 10^{-6}$ (m)	From manufacturer
Fuel electrode thickness	$25 \cdot 10^{-6}$ (m)	From manufacturer
Tortuosity	4	[31]
Porosity	0.35	[31]
Boltzmann's constant	$1.380649 \cdot 10^{-23}$ (J/K)	
Mean characteristic length of hydrogen	$2.827 \cdot 10^{-10}$ (m)	[32]
Mean characteristic length of water	$2.641 \cdot 10^{-10}$ (m)	[32]
Mean characteristic length of oxygen	$3.467 \cdot 10^{-10}$ (m)	[32]
Mean characteristic length of nitrogen	$3.798 \cdot 10^{-10}$ (m)	[32]
Lennard-Jones characteristic energy of hydrogen	$8.24 \cdot 10^{-22}$ (J)	[32]
Lennard-Jones characteristic energy of water	$1.12 \cdot 10^{-20}$ (J)	[32]
Lennard-Jones characteristic energy of nitrogen	$9.86 \cdot 10^{-22}$ (J)	[32]
Lennard-Jones characteristic energy of oxygen	$1.47 \cdot 10^{-21}$ (J)	[32]
Dynamic viscosity at reference temperature	$5.09 \cdot 10^{-5}$ (Pa s)	[32]
A	1.06306	[32]
B	0.1561	[32]
C	0.193	[32]
D	0.47635	[32]
E	1.03587	[32]
F	1.52996	[32]
G	1.76474	[32]
H	3.89411	[32]

resistance (corresponding to 0.368 and 0.432 Ω cm^2 of ASR), and 0.006 and 0.052 Ω of polarisation resistance (corresponding to 0.096 and 0.832 Ω cm^2 of ASR) obtained in SOEC and SOFC modes, respectively, most likely due to different degradation states of the cell, together with possible variations in contact resistance and interfacial conditions during the experimental campaign.

Figs. 4(a), 4(b) show the EIS spectra recorded when varying the water content in the fuel electrode with respect to the reference conditions in SOEC and SOFC modes. As can be noticed, the spectra in SOEC mode became larger and more dispersed with the increased water content; furthermore, the ohmic resistance slightly increased. This is due to the increase of the water vapour content into the fuel mixture, which has a strong influence on the polarisation and ohmic resistance of the electrode [33]; indeed, a high level of humidity into the feeding gas could lead to a Nickel depletion phenomenon at the electrode-electrolyte interface, which in turn causes the fuel electrode degradation, as demonstrated in [9,19], where it was shown that high steam contents significantly accelerate Ni depletion and fuel-electrode microstructural degradation, leading to pronounced modifications of the high-frequency impedance arcs associated with partial Ni oxidation. In addition, a partial oxidation of the fuel electrode could occur due to the presence of a high water quantity (e.g., 90% of steam). However, during the experimental tests no abnormal behaviour was observed, as the cell voltage remained stable and no significant drift or sudden performance loss occurred within the measurement timescale. This is also reflected in an increase of the cell's resistance at high (ohmic resistance) and low (polarisation resistance) frequencies. Furthermore, the presence of high water vapour fractions may locally reduce effective gas diffusivity within the porous electrode, due to pore blockage and/or condensation phenomena, thereby enhancing low-frequency polarisation losses, as discussed in [7,32]. The heat exchange between the water vapour and the cell's components also leads to a decrease in the electrolyte temperature, and thus an increase of the cell's ohmic resistance should be considered.

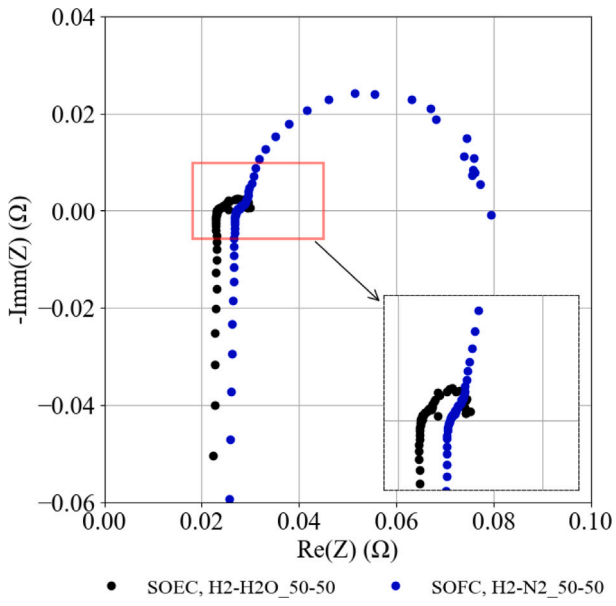

Fig. 3. EIS spectra in SOEC and SOFC reference conditions. The inset shows enlarged views of selected impedance regions, including the high-frequency region used to inspect the ohmic intercept.

In SOFC mode, an opposite behaviour is observed: the ohmic resistance remains nearly constant when varying the water content, while the polarisation resistance is higher at the lowest water vapour concentration. In this operating mode, water is not directly required for the electrochemical reaction, and therefore experimental tests were

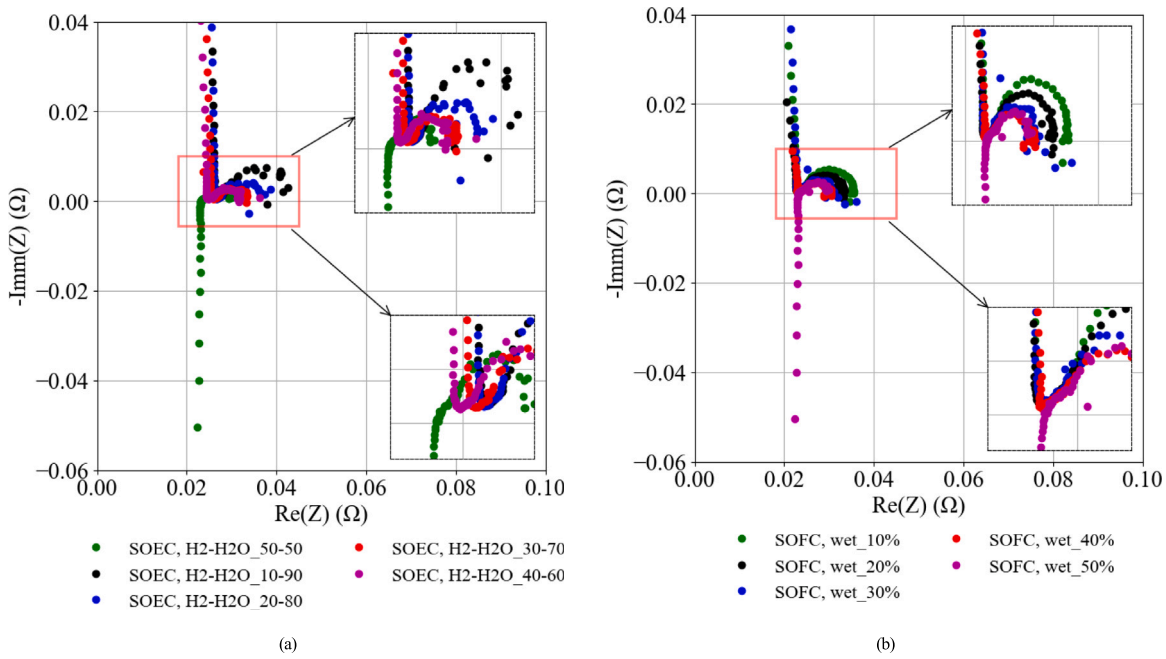

Fig. 4. EIS spectra at different steam contents at the fuel electrode: (a) SOEC mode; (b) SOFC mode. Insets show enlarged views of selected impedance regions, including the high-frequency region used to inspect the ohmic intercept.

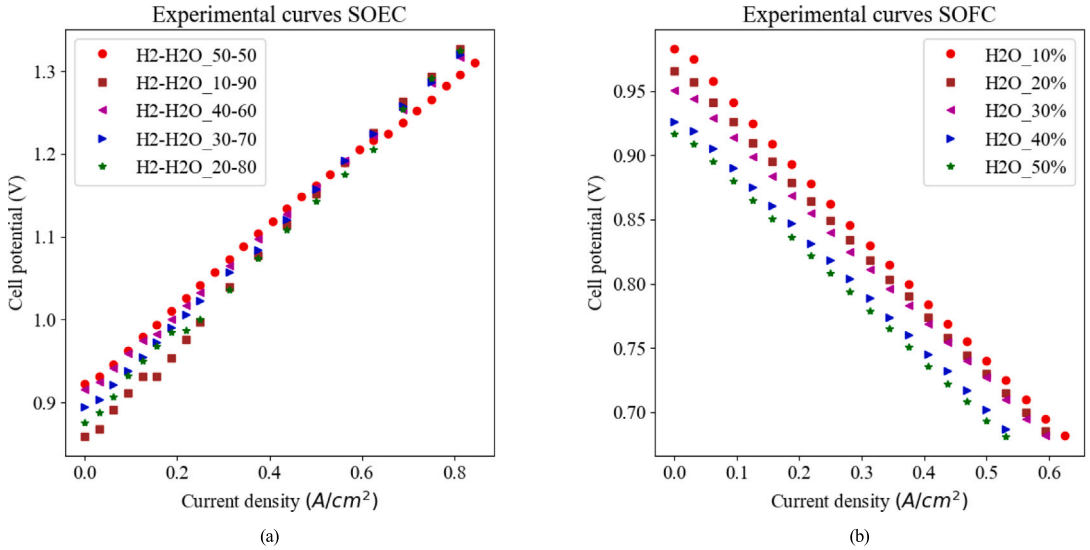

Fig. 5. Experimental polarisation curves at different steam contents at the fuel electrode: (a) SOEC mode; (b) SOFC mode.

limited to water vapour contents up to 50%. This experimental range reduces the possibility of directly observing phenomena comparable to those identified under high-humidity SOEC conditions. When the EIS resistances are expressed in ASR form, the same trends are confirmed, indicating that the observed variations are associated with the operating conditions rather than with geometrical effects related to cell area.

Although similar effects could potentially arise at higher water vapour concentrations also in SOFC mode, such behaviour was not experimentally investigated in the present study and is therefore identified as a relevant direction for future work aimed at fully assessing the impact of extreme water contents on the cell behaviour.

Fig. 5(a), 5(b) show the polarisation curves obtained in the experiments in both SOEC and SOFC modes, respectively, when varying the water content at the fuel electrode. As can be noticed, the trend of the polarisation curves reflects what was obtained from the spectra; indeed, the slope of the experimental curves in SOEC mode varies with the water concentration, indicating that there is a variation of the cell's internal resistance. In SOFC mode, the experimental curves show the same slope in each water content level tested, thus indicating that the cell's internal resistance remains constant despite the feeding mixture at the fuel electrode. Based on the maximum current densities reached during the tests, the estimated fuel utilisation factor in SOFC mode was about 45%, while the steam utilisation factor in SOEC mode ranged approximately from 33% to 59% depending on the inlet H_2O fraction. Therefore, concentration polarisation could not be excluded a priori, especially at the highest current densities, thus justifying the retention of concentration overpotential terms in the semi-empirical numerical model.

It is worth noting that, from the polarisation curves, only the ohmic contribution of the cell's resistance is analysed, being representative of

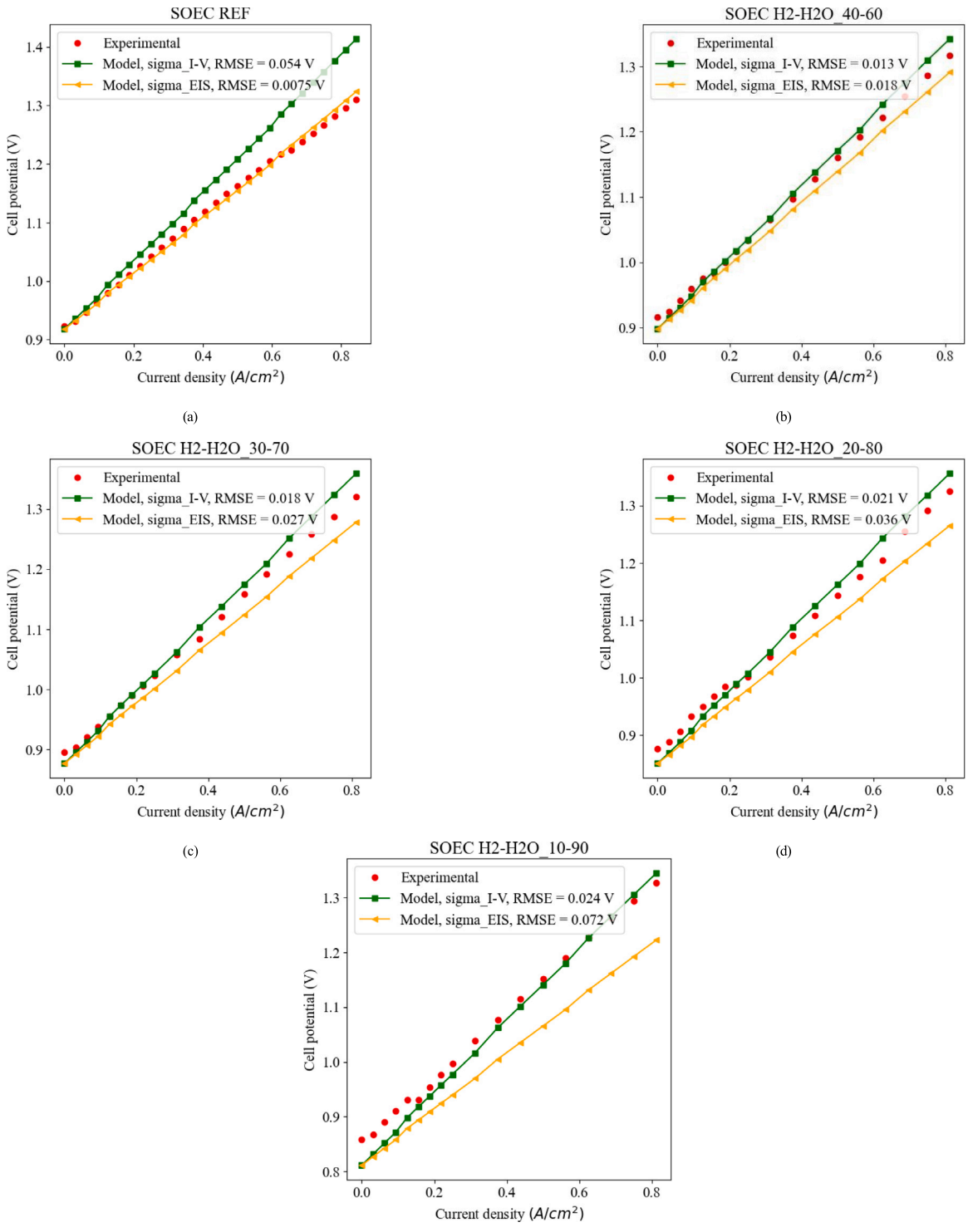

Fig. 6. Semi-empirical model validation in SOEC mode at different water contents at the fuel electrode: (a) 50% (reference), (b) 60%, (c) 70%, (d) 80%, (e) 90%.

the global system's behaviour without any possibility of separating the different electrochemical processes occurring within the cell.

From the data recorded, an effective conductivity parameter was obtained for each operating condition. Tables 6 and 7 show the values derived from the EIS spectra and polarisation curves for both operating modes. It should be noted that the reported conductivity variations should mainly be interpreted as changes in the effective parameter extracted from EIS spectra or polarisation curves, rather than direct modifications of the intrinsic electrolyte material property.

Table 6
Electrolyte conductivity values in SOEC mode. PC = polarisation curve method; EIS = Electrochemical Impedance Spectroscopy.

Fuel composition (H_2–H_2O%)	50–50	40–60	30–70	20–80	10–90
σ PC (S/cm)	0.017	0.018	0.016	0.015	0.014
σ EIS (S/cm)	0.022	0.021	0.020	0.019	0.019

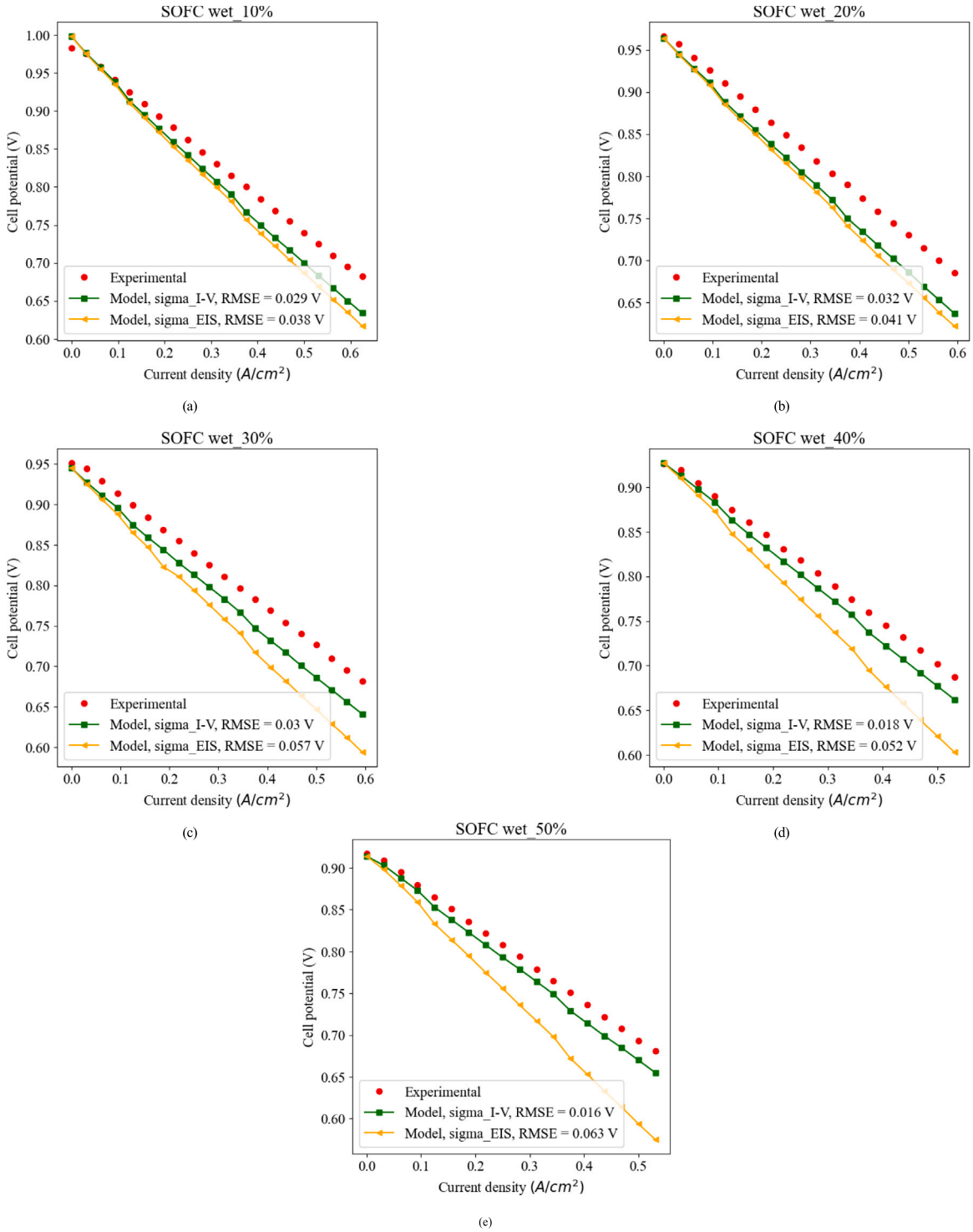

Fig. 7. Semi-empirical numerical model validation in SOFC mode at different water contents at the fuel electrode: (a) 10%, (b) 20%, (c) 30%, (d) 40%, and (e) 50%.

Table 7
Electrolyte conductivity values in SOFC mode. PC = polarisation curve method; EIS = Electrochemical Impedance Spectroscopy.

Fuel humidification percentage (%)	10	20	30	40	50
σ PC (S/cm)	0.018	0.018	0.019	0.019	0.019
σ EIS (S/cm)	0.017	0.017	0.016	0.015	0.014

3.2. Semi-empirical numerical model validation

The semi-empirical numerical model described in Section 2 was validated with experimental data shown in Figs. 5(a) and 5(b) using, in each operating condition, the electrolyte conductivity derived from both the corresponding EIS spectrum and polarisation curve in both cell's operating modes. Results in SOEC mode are displayed in Fig. 6.

As can be noticed in Fig. 6(a), when the system is operating at reference conditions in SOEC mode, the conductivity obtained from the

EIS spectrum is more accurate than that obtained from the polarisation curves; indeed, the conductivity value from the EIS spectrum led to a Root Mean Square Error (RMSE) between the experimental points and the simulated curve of 0.0075 V, while the one obtained with the conductivity calculated from the experimental polarisation curve is 0.054 V. From this condition on, as the water content within the fuel mixture increases, the predicted curve obtained using the conductivity value derived from the EIS spectrum progressively deviates from the experimental data. On the other hand, the predicted curve obtained with the conductivity value from the experimental polarisation curves improved by getting closer to the experimental points. This was also confirmed by the RMSE values that, in the first case, were always higher. The worst scenario was represented by a fuel mixture with a water content of 90%; indeed, the RMSE value was the highest and equal to 0.072 V. This behaviour is consistent with the observations discussed above: at high water concentrations, the EIS spectrum becomes larger and more dispersed. Furthermore, high steam fractions may promote changes in the fuel electrode condition, such as partial Ni re-oxidation or interfacial modifications, which can affect the apparent internal resistance. This behaviour should not be interpreted as a direct variation of the intrinsic electrolyte material property. Rather, changes in steam content modify electrode kinetics, gas transport conditions, and interfacial contributions, which in turn affect the effective conductivity parameter estimated from EIS or polarisation data. On the contrary, polarisation curves provide a global measurement of the overall cell voltage response. Therefore, conductivity values derived from their slope are less sensitive to uncertainties associated with separating individual impedance contributions, resulting in more robust model calibration at high steam content. Same results obtained in SOFC mode are shown in Fig. 7 below.

Also in the SOFC mode, the higher the water content within the fuel mixture, the lower the reliability of the curve obtained from the semi-empirical numerical model with the electrolyte conductivity taken from the EIS spectra. This is confirmed by RMSE values that were always higher than those calculated with the polarisation curves method. In this case, even if the spectra showed an improvement with the increase of the water content, internal phenomena like the cooling of the cell, which were due to the temperature difference between the water vapour and the cell's components, led to an underestimation of the electrolyte conductivity derived from the spectra, thus affecting the accuracy of the semi-empirical numerical model. It is worth noting that, although recalibrating the model parameters at each humidity condition could reduce the local prediction error, the present analysis intentionally evaluates the robustness of a common parameter set under varying steam contents.

4. Conclusions

This work investigates the influence of water content in the fuel mixture of a rSOC on electrolyte conductivity estimation methods, as obtained from both EIS and polarisation curve measurements. A semi-empirical numerical model of the electrochemical system was used to simulate and predict its behaviour in both SOEC and SOFC operating modes, when embedding the experimentally derived conductivity values.

Water vapour concentrations up to 90% in SOEC mode and 50% in SOFC mode were tested. For each operating condition, both an EIS spectrum and a polarisation curve were recorded, and electrolyte conductivity values were extracted from both methods and used to validate the semi-empirical model.

Results showed that in SOEC mode, water vapour contents above 50% lead to broader and more dispersed EIS spectra, increasing both polarisation and ohmic resistance. This reduces the reliability of conductivity parameters derived from EIS, resulting in decreased model accuracy. In SOFC mode, while EIS spectra improve with increasing water content, internal cooling effects, caused by temperature differences between water vapour and cell components, can lead to an underestimation of conductivity, again lowering model precision. EIS is a sensitive and powerful technique for identifying electrochemical phenomena within the cell, and is generally preferred over polarisation curves, which only reflect the overall system behaviour without distinguishing individual processes. However, under specific conditions such as high water vapour content, EIS-derived parameter estimation may become less accurate. In such cases, polarisation curves offer a more robust means of assessing system behaviour across varying conditions.

The quantitative results reported in this work are specific to the investigated electrolyte-supported cell. However, the general methodological conclusion that fuel-side humidity may affect conductivity parameter estimation and model calibration may be transferable to other SOC architectures, including anode-supported cells, although with different magnitudes and dominant mechanisms. Moreover, inaccurate conductivity parameterisation at cell level may propagate into errors in voltage prediction, efficiency estimation, thermal management, and control-oriented digital-twin frameworks used for stack-level modelling and system integration.

The present study is subject to some limitations, as it was performed on a single commercial ESC cell at fixed operating temperature, without a dedicated repeatability campaign or multi-temperature validation. Therefore, the conclusions should be interpreted within the investigated operating range, while broader generalisation requires further experimental assessment.

Future work will include extended experimental campaigns, multi-temperature validation, and application of the proposed methodology to stack and system-level analyses under realistic operating scenarios.

CRediT authorship contribution statement

Francesca Mennilli: Writing – review & editing, Writing – original draft, Visualization, Validation, Software, Methodology, Investigation, Formal analysis, Data curation, Conceptualization. **Mosè Rossi:** Writing – review & editing, Writing – original draft, Visualization, Methodology, Formal analysis, Conceptualization. **Andrea Monforti Ferrario:** Methodology, Investigation, Conceptualization. **Massimiliano Della Pietra:** Writing – review & editing, Writing – original draft, Supervision, Resources, Project administration, Funding acquisition. **Gabriele Comodi:** Writing – review & editing, Writing – original draft, Supervision.

Declaration of competing interest

The authors declare that they have no known competing financial interests or personal relationships that could have appeared to influence the work reported in this paper.

Acknowledgements

This research was funded by the European Union - NextGenerationEU from the Italian Ministry of Environment and Energy Security, POR H2 AdP MEES/ENEA with involvement of CNR and RSE, PNRR - Mission 2, Component 2, Investment 3.5 "Ricerca e sviluppo sull'idrogeno", CUP: I83C22001170006.

Data availability

Data will be made available on request.

References

[1] N. Hassan, A. Jalil, S. Rajendran, N. Khusnun, M. Bahari, A. Johari, M. Kamaruddin, M. Ismail, Recent review and evaluation of green hydrogen production via water electrolysis for a sustainable and clean energy society, Int. J. Hydrog. Energy 52 (Part B) (2024) 420–441, http://dx.doi.org/10.1016/j.ijhydene.2023.09.068.

[2] A. Irham, M. Roslan, K.P. Jern, M. Hannan, T.I. Mahlia, Hydrogen energy storage integrated grid: A bibliometric analysis for sustainable energy production, Int. J. Hydrog. Energy 63 (2024) 1044–1087, http://dx.doi.org/10.1016/j.ijhydene.2024.03.235.

[3] F. Mennilli, L. Jin, M. Rossi, G. Comodi, Assessment of a NaOH-based alkaline electrolyser's performance: System modelling and operating parameters optimisation, Int. J. Hydrog. Energy 85 (2024) 625–634, http://dx.doi.org/10.1016/j.ijhydene.2024.08.175.

[4] M.F. Vostakola, H. Ozcan, R.S. El-Emam, B.A. Horri, Recent advances in high-temperature steam electrolysis with solid oxide electrolysers for green hydrogen production, Energies 16 (2023) 3327, http://dx.doi.org/10.3390/en16083327.

[5] S. Frangini, Celle a combustibile a carbonati fusi per la cattura di CO2 da gas combusti: prospettive e limiti di applicazione in settori industriali soggetti alla direttiva EU-ETS, Ric. Sist. Elettr. (2010).

[6] A. Camaioni, Analisi comparativa di sistemi enrgetici integrati con celle a combustibile, Tesi Laurea Impatto Ambient. Dei Sist. Energetici (A.Y. 2010/2011).

[7] P. Kim, D. Brett, N. Brandon, The effect of water content on the electrochemical impedance response and microstructure of Ni-CGO anodes for solid oxide fuel cells, J. Power Sources 189 (2009) 1060–1065, http://dx.doi.org/10.1016/j.jpowsour.2008.12.150.

[8] O.B. Rizvandi, R.J. Braun, Distinct modeling parameter identification for precision modeling of solid oxide cells under fuel cell and electrolysis modes, J. Power Sources 653 (237716) (2025) http://dx.doi.org/10.1016/j.jpowsour.2025.237716.

[9] M.P. Hoerlein, M. Riegraf, R. Costa, G. Schiller, K.A. Friedrich, A parameter study of solid oxide electrolysis cell degradation: Microstructural changes of the fuel electrode, Electrochim. Acta 258 (2018) 162–175, http://dx.doi.org/10.1016/j.electacta.2018.04.170.

[10] M. Hauck, S. Herrmann, H. Spliethoff, Simulation of a reversible SOFC with Aspen Plus, Int. J. Hydrog. Energy 42 (2017) 10329–10340, http://dx.doi.org/10.1016/j.ijhydene.2017.01.189.

[11] S. Ihara, S. Naruse, H. Muroyama, T. Matsui, Wettability analysis of Ni/YSZ interface under operating conditions of solid oxide cells, J. Power Sources 654 (237867) (2025) http://dx.doi.org/10.1016/j.jpowsour.2025.237867.

[12] J. Grimes, J. Hong, S.A. Barnett, Effect of Gd-doped ceria infiltration into Ni-YSZ on reversible solid oxide cell operation, J. Power Sources 551 (232189) (2022) http://dx.doi.org/10.1016/j.jpowsour.2022.232189.

[13] E.D.R. Silva, G. Sassone, M. Prioux, M. Hubert, B. Morel, J. Laurencin, A multiscale model validated on local current measurements for understanding the solid oxide cells performances, J. Power Sources 556 (232499) (2023) http://dx.doi.org/10.1016/j.jpowsour.2022.232499.

[14] H. Zheng, Y. Tian, L. Zhang, B. Chi, J. Pu, L. Jian, La0.8Sr0.2Co0.8Ni0.2O3-δ impregnated oxygen electrode for H2O/CO2 coelectrolysis in solid oxide electrolysis cells, J. Power Sources 383 (2018) 93–101, http://dx.doi.org/10.1016/j.jpowsour.2018.02.041.

[15] B. Song, E. Ruiz-Trejo, A. Bertei, N.P. Brandon, Quantification of the degradation of Ni-YSZ anodes upon redox cycling, J. Power Sources 374 (2018) 61–68, http://dx.doi.org/10.1016/j.jpowsour.2022.232499.

[16] A. Martos, S. Márquez, R. Pavlov, W. Zambelli, S. Anelli, M. Nuñez, L. Bernadet, J. Brey, M. Torrell, A. Tarancón, 3D printing of reversible solid oxide cell stacks for efficient hydrogen production and power generation, J. Power Sources 609 (234704) (2024) http://dx.doi.org/10.1016/j.jpowsour.2024.234704.

[17] M. Pagliari, D. Montinaro, E. Martelli, S. Campanari, A. Donazzi, Durability and kinetic effects of CO2-rich oxidizing streams on LSCF-based solid oxide fuel cells, J. Power Sources 613 (234895) (2024) http://dx.doi.org/10.1016/j.jpowsour.2024.234895.

[18] A. Akter, J.R. Mulligan, H. Grande, U. Pal, S.N. Basu, S. Gopalan, Reversible solid oxide cells: Early performance and microstructural evolution during electrolysis and switched mode operation, J. Power Sources 572 (233093) (2023) http://dx.doi.org/10.1016/j.jpowsour.2023.233093.

[19] S. Wang, X. Hao, W. Zhan, Research on a low temperature reversible solid oxide cell, Int. J. Hydrog. Energy 42 (2017) 29881–29887, http://dx.doi.org/10.1016/j.ijhydene.2017.09.181.

[20] S.A. Inc., ZView 4.0, Impedance/Gain Phase, Graphing and Analyisis Software, Scribner Associates Inc., 2023.

[21] Q.-A. Huang, R. Hui, B. Wang, J. Zhang, A review of AC impedance modeling and validation in SOFC diagnosis, Electrochem. Acta 52 (2007) 8144–8164, http://dx.doi.org/10.1016/j.electacta.2007.05.071.

[22] C. Boigues Muñoz, Computational Simulation of Solid Oxide Fuel Cells – Integrating numerical and experimental approaches (Ph.D. thesis), Università Politecnica Delle Marche, 2015.

[23] M. Carmo, D.L. Fritz, J. Mergel, D. Stolten, A comprehensive review on PEM water electrolysis, Int. J. Hydrog. Energy 38 (2013) 4901–4934, http://dx.doi.org/10.1016/j.ijhydene.2013.01.151.

[24] D. Falcão, A. Pinto, A review on PEM electrolyzer modelling: Guidelines for beginners, J. Clean. Prod. 261 (2020) 121184, http://dx.doi.org/10.1016/j.jclepro.2020.121184.

[25] R. O'Hayre, S.-W. Cha, W.G. Colella, F.B. Prinz, Fuel Cell Fundamentals, John Wiley & Sons, Hoboken, New Jersey, 2009.

[26] N. Sammes, Fuel Cell Technology: Reaching Towards Commercalization, Springer, London, 2006.

[27] C. Bao, Z. Jiang, X. Zhang, Modeling mass transfer in solid oxide fuel cell anode: I. Comparison between Fickian, Stefan–Maxwell and dusty-gas models, J. Power Sources 310 (2016) 32–40.

[28] M. Ni, M.K. Leung, D.Y. Leung, A modeling study on concentration over potentials of a reversible solid oxide fuel cell, J. Power Sources 163 (2006) 460–466, http://dx.doi.org/10.1016/j.jpowsour.2006.09.024.

[29] F.R. Bianchi, A.K. Padinjarethil, A. Hagen, B. Bosio, Multiscale analysis of Ni-YSZ and Ni-CGO anode based SOFC degradation: From local microstructural variation to cell electrochemical performance, Electrochim. Acta 460 (2023) 142589, http://dx.doi.org/10.1016/j.electacta.2023.142589.

[30] R.D. Loss, Atomic weights of the elements 2001 (IUPAC technical report), Pure Appl. Chem. 75 (8) (2003) 1107–1122.

[31] A.K. Padinjarethil, F.R. Bianchi, B. Bosio, A. Hagen, Electrochemical characterization and modelling of anode and electrolyte supported solid oxide fuel cells, Front. Energy Res. 9 (668964) (2021) http://dx.doi.org/10.3389/fenrg.2021.668964.

[32] R.C. Reid, J.M. Prausnitz, B.E. Poling, The Properties of Gases & Liquids, McGraw-Hill Companies, 1987.

[33] A. Nechache, M. Cassir, A. Ringuedé, Solid oxide electrolysis cell analysis by means of electrochemical impedance spectroscopy: A review, J. Power Sources 258 (2014) 164–181, http://dx.doi.org/10.1016/j.jpowsour.2014.01.110.